Spatio-temporal behaviour in an enclosed corotating disk pair

By ANTHONY RANDRIAMAMPIANINA[1],
ROLAND SCHIESTEL[1] AND MICHAEL WILSON[2]

[1]Institut de Recherche sur les Phénomènes Hors Equilibre, UMR 6594 CNRS,
Technopôle de Château-Gombert, 49 rue F. Joliot Curie, 13384 Marseille cedex 13, France

[2]Department of Mechanical Engineering, Faculty of Engineering and Design, University of Bath,
Bath BA2 7AY, UK

We present a numerical investigation of the flow between corotating disks with a stationary outer casing – the enclosed corotating disk pair configuration. It is known that in such a geometry, axisymmetric and three-dimensional flow regimes develop depending on the value of the rotation rate. The three-dimensional flow is always unsteady owing to its wavy structure in the radial-tangential plane. Axisymmetric regimes exhibit first a pitchfork bifurcation, characterized by a symmetry breaking with respect to the inter-disk midplane, before a Hopf bifurcation is established. The regime diagrams for these bifurcations are given in the (Re, G)-plane, where $Re(= \Omega b^2/v)$ is the rotational Reynolds number and $G(= s/(b-a))$ is the gap ratio. For values of G smaller than a critical limit $G_c \sim 0.26$, there exists a range of rotation rates where the motion becomes time-dependent before bifurcating to a steady symmetry breaking regime. It is shown that for $G \geqslant G_c$ the transition to unsteady three-dimensional flow occurs after the pitchfork bifurcation, and the flow structure is characterized by a shift-and-reflect symmetry. The transition to three-dimensional flow is consistent with experimental observations made by Abrahamson *et al.* (1989) where multiple solutions develop (known as the intransitivity phenomenon) with the presence of quasi-periodic behaviour resulting from successive vortex pairings. On the other hand, for smaller values of gap ratio, the three-dimensional flow shows a symmetry breaking. Finally, it is found that the variation of torque coefficient as a function of the rotation rate is the same for both the axisymmetric and three-dimensional solutions.

1. Introduction

The enclosed corotating disk pair (ECDP) configuration is formed (as illustrated in figure 1) by two corotating disks delimited by an inner cylinder, the hub, corotating with the disks and an outer, stationary casing. Applications include mainly computer disk storage systems and disk cavities in turbomachinery. The geometry considered here is characterized by a large hub radius ratio: $a/b \geqslant 0.5$, where a and b are the inner and outer radius. The present numerical study is concerned with the spatio-temporal behaviour of the flow developing during the different bifurcations observed in such configurations, and in particular with the transition to three-dimensional flow.

Previous numerical work related to the ECDP configuration (Herrero, Giralt & Humphrey 1995) has reported that the transition to three-dimensional flow occurs
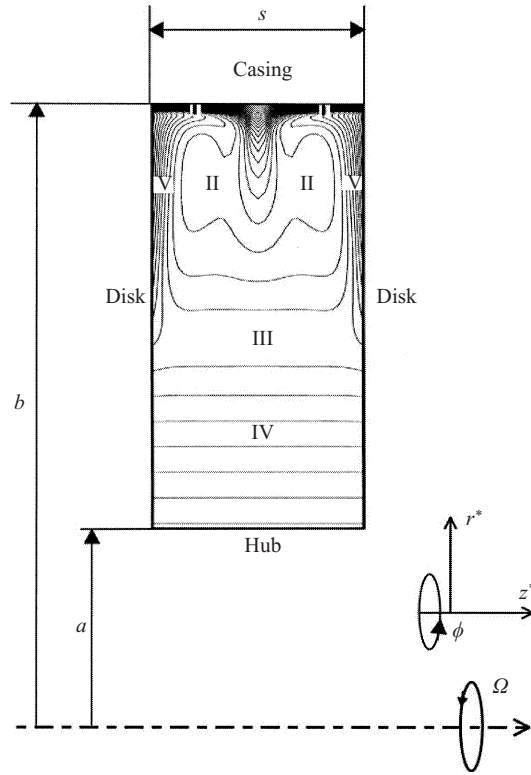
FIGURE 1. Schematic diagram of the ECDP section with relevant dimensions and definition of the five regions in the (r, z)-plane (based on Schuler *et al.* 1990).

with unsteady motion, induced by wavy structures in the radial-tangential plane, with a drift ranging between 0.5 and 0.8 of the angular velocity of the disks (Herrero *et al.* 1999). Similar behaviour has been observed during the development of baroclinic waves in a differentially heated rotating annulus (Fowlis & Hide 1965; Hignett *et al.* 1985). In the case of baroclinic flows, the wave patterns are characterized by a 'jet-stream' moving between cyclonic and anticyclonic vortices, with a characteristic meandering structure occupying the whole cavity. In the present case, the vortices are restricted to a region located close to the stationary outer cylinder, while the inner region is mainly governed by the Taylor–Proudman theorem (solid-body rotation). Moreover, previous workers have reported that the number of structures decreases in a stepwise manner with increasing rotation rate, whereas for the baroclinic waves, it increases with the rotation rate.

   Abrahamson, Eaton & Koga (1989) used flow visualization to show the vortical structures for an ECDP with small gap ratio, $0.026 \leqslant G \leqslant 0.2$, with radius ratio $a/b = 0.5$. They considered water as the working fluid for a range of rotational Reynolds number $1.5 \times 10^5 \leqslant Re = \Omega b^2/\nu \leqslant 1.5 \times 10^6$. They observed three distinct regions: an inner region characterized by solid-body rotation near the hub, an outer region (core) dominated by large counter-rotating vortices and the shroud boundary layer. They showed, in particular, the polygonal shape of the boundary separating the inner region from the outer region, resulting from the presence of the outer vortices. From their experiments in a configuration formed by two corotating coaxial disks, for a range of gap ratio $0.08 \leqslant S = s/b \leqslant 1.28$, Akhmetov & Tarasov (1987) reported

that when a critical Reynolds number is exceeded, the limit of the inner region takes on the form of an oval, triangle, quadrangle, etc. When varying the rotation rate for $G = 0.1$, Abrahamson *et al.* (1989) obtained the successive occurrence of three regimes: indeterminate characterized by different pairings of vortices, alternating vortex states and finally stable vortices. For the second regime, the flow structure alternately exhibited different states under the same physical conditions, known as the intransitivity phenomenon (Fowlis & Hide 1965; Hignett *et al.* 1985), although the flow became more stable than for the first regime. Abrahamson *et al.* (1989) found that the number of structures in the outer region decreased in a stepwise manner, and the level of relative motion in the inner region increased. They also mentioned the presence of vortical structures in the inner region at high rotation rates and large axial separation.

In experiments with air, Schuler *et al.* (1990) delineated, in a fixed geometry with $G = 0.196$ and $a/b = 0.537$, five distinct flow regions (see figure 1) for large values of the rotation rate, $2.22 \times 10^4 \leqslant Re \leqslant 2.66 \times 10^5$: the region near the hub in solid-body rotation (denoted region IV), the boundary layer close to the fixed shroud (region I), the inviscid core (region II) characterized by negligible gradients in the radial and axial directions, region III corresponding to the transition between region II and IV, and the Ekman layers along the two disks (region V). The core region is composed of two separate zones in the meridional plane, which may or may not exhibit symmetry with respect to the inter-disk midplane. Region III (visualized by Abrahamson *et al.* (1989) as a polygon in the (r, ϕ)-plane, see also Humphrey & Gor (1993)) constitutes a detached shear layer, resulting from the meeting of the three-dimensional vortical structures in region II with the two-dimensional flow in region IV (which satisfies the Taylor–Proudman theorem). This separation is found to act like a compliant surface, owing to the solid-body rotation of the inner region (Schuler *et al.* 1990; Humphrey & Gor 1993). Humphrey & Gor (1993) provided quantitative data for the radial location and thickness of this region from experiments.

Humphrey, Schuler & Webster (1995) carried out numerical studies using finite-difference approximations for the configuration considered by Schuler *et al.* (1990). They found that the number of vortices in region II appeared to be an even integer, because the wavelength of the tangential velocity component, responsible for the nodal distribution of axial vorticity, is twice that for the axial velocity component. Using an improved version of this method and using a refined grid, Iglesias & Humphrey (1998) obtained three-dimensional solutions showing a symmetry breaking with respect to the inter-disk midplane, in addition to the shift-and-reflect symmetry structure observed by Humphrey *et al.* (1995) when considering different aspect ratios. In recent studies using the same numerical formulation, Herrero, Giralt & Humphrey (1999) reported the effect of gap ratio on two-dimensional–three-dimensional transition. They produced a regime diagram showing the existence of two different families of unsteady three-dimensional flow: (*a*) for sufficiently large values of G, a three-dimensional flow that is asymmetric with respect to the inter-disk midplane (denoted regime III); (*b*) for smaller gap ratio, a three-dimensional flow that displays shift-and-reflect symmetry with respect to the inter-disk midplane (regime II). Both families of flows are characterized by distinct behaviour in frequency/wavelength transitions. However, the second family develops for a range of rotation rates before bifurcating to the first one. Herrero *et al.* (1999) also found that regime III is characterized by the polygonal boundary of region II, as visualized by Abrahamson *et al.* (1989).

Experimental and computational studies for a large value of gap ratio ($G = 0.6$) and at high rotation rates have been carried out at the University of Bath (Gan *et al.*

1996; Mirzaee, Wilson & Owen 1997; Lewis, Rees & Wilson 1998). Gan *et al.* (1996) identified a Rankine (combined free and forced) vortex structure for the measured flow (see also Owen & Rogers 1995).

In the present work, the effect of rotation rate on the different flow regimes is analysed for different gap ratios $0.1 \leqslant G \leqslant 0.6$. The present study complements the numerical work carried out for smaller gap ratio by Herrero *et al.* (1999). The curvature parameter $R_c = (b + a)/(b - a)$ was kept at $R_c = 3$ ($a/b = 0.5$) for all the simulations reported. This corresponds to the value considered by Abrahamson *et al.* (1989) and also at the University of Bath, and is slightly smaller than the one studied in Schuler *et al.* (1990) and Humphrey & Gor (1993), $R_c = 3.32$.

2. Mathematical model

The motion is governed by the incompressible Navier–Stokes equations. In a fixed stationary frame of reference, the dimensionless momentum equations can be written as:

$$\frac{\mathrm{D}V_r}{\mathrm{D}t} - G\frac{V_\phi^2}{(r + R_c)} = -G\frac{\partial p}{\partial r} + \frac{(R_c + 1)}{GRe}$$
$$\left(\nabla^2 V_r - G^2\frac{V_r}{(r + R_c)^2} - \frac{2G^2}{(r + R_c)^2}\frac{\partial V_\phi}{\partial \phi} \right), \quad (2.1)$$

$$\frac{\mathrm{D}V_\phi}{\mathrm{D}t} + G\frac{V_r V_\phi}{(r + R_c)} = -\frac{G}{(r + R_c)}\frac{\partial p}{\partial \phi} + \frac{(R_c + 1)}{GRe}$$
$$\left(\nabla^2 V_\phi - G^2\frac{V_\phi}{(r + R_c)^2} + \frac{2G^2}{(r + R_c)^2}\frac{\partial V_r}{\partial \phi} \right), \quad (2.2)$$

$$\frac{\mathrm{D}V_z}{\mathrm{D}t} = -\frac{\partial p}{\partial z} + \frac{(R_c + 1)}{GRe}\nabla^2 V_z, \quad (2.3)$$

where,

$$\frac{\mathrm{D}V}{\mathrm{D}t} = \frac{\partial V}{\partial t} + \tfrac{1}{2}(V\nabla \cdot V + \nabla(V \cdot V)), \quad (2.4)$$

$$\nabla^2 = G^2\frac{1}{(r + R_c)}\partial\left(r\frac{\partial}{\partial r}\right) + G^2\frac{1}{(r + R_c)^2}\frac{\partial^2}{\partial \phi^2} + \frac{\partial^2}{\partial z^2}. \quad (2.5)$$

The mass conservation equation is:

$$G\frac{1}{(r + R_c)}\frac{\partial r V_r}{\partial r} + G\frac{1}{(r + R_c)}\frac{\partial V_\phi}{\partial \phi} + \frac{\partial V_z}{\partial z} = 0. \quad (2.6)$$

$Re = \Omega b^2/v$ is the rotational Reynolds number, with v the kinematic viscosity. The velocity, pressure and time scalings correspond to Ωb, $\tfrac{1}{2}\rho\Omega^2 b^2$ and $s/2b\Omega$, respectively. In the meridional plane, the space variables $(r^*, z^*) \in [a, b] \times [0, s]$ (see figure 1) have been normalized into the square $[-1, 1] \times [-1, 1]$, a requisite for the use of Chebyshev polynomials:

$$r = \frac{2r^*}{b - a} - R_c, \quad z = \frac{2z^*}{s} - 1. \quad (2.7)$$

The 'skew-symmetric' form proposed by Zang (1990) was chosen for the convective

terms in the momentum equations (2.4) to ensure the conservation of kinetic energy, a necessary condition for a simulation to be numerically stable in time.

The inner cylinder and the two disks rotate with the same angular velocity Ω, while the outer cylinder is fixed. However, in order to maintain the spectral accuracy of the solution, a regularization is introduced for the tangential velocity component at the discontinuity between the disks and the casing (see Randriamampianina *et al.* 1997). For the same configuration, but with a large aspect ratio ($2 \leqslant G \leqslant 4$) for Taylor–Couette problems, Tavener, Mullin & Cliffe (1991) mentioned that the effects on the flow patterns away from the corners are negligible if a clearance δ between the disk and casing is considered which remains sufficiently small ($\delta/b < 0.02$). This clearance is small in the experiments reported in literature related to the present studies ($\delta/b = 0.036$ in Abrahamson *et al.* (1989), and $\delta/b = 0.026$ in Schuler *et al.* (1990) and Humphrey & Gor (1993)).

For the axisymmetric regimes ($\partial/\partial\phi = 0$), a vorticity ($\zeta$)–streamfunction ($\psi$) formulation with the azimuthal velocity (V_ϕ) was preferred to the use of primitive variables (Chaouche, Randriamampianina & Bontoux 1990).

3. Solution method

3.1. *Temporal scheme*

The time integration used is second-order accurate and is based on a combination of Adams–Bashforth (AB) and backward differentiation formula (BDF) schemes, chosen for its good stability properties (Vanel, Peyret & Bontoux 1986). The resulting AB/BDF scheme is semi-implicit, and for the transport equation of any dependent variable f ($f = V_r, V_\phi, V_z$ for three-dimensional regimes and $f = \zeta, V_\phi$ for axisymmetric ones) can be written as:

$$\frac{3f^{l+1} - 4f^l + f^{l-1}}{2\delta t} + 2N(f^l) - N(f^{l-1}) = -A\frac{\partial p^{l+1}}{\partial n} + \frac{(R_c + 1)}{GRe}\nabla^2 f^{l+1}, \qquad (3.1)$$

where $N(f)$ represents nonlinear terms, n is the normal direction, δt is the timestep and the superscript l refers to time level ($A = 0$ for the axisymmetric formulation). For the three-dimensional solution, the cross-terms in the diffusion part in the (r, ϕ)-plane resulting from the use of cylindrical coordinates in (2.1)–(2.2) are treated within $N(f)$, in order to maintain an overall second-order time accuracy (Le Quéré & Pécheux 1990).

For the initial step, we have taken $f^{-1} = f^0$. At each timestep, the problem then reduces to the solution of Helmholtz and Poisson equations.

3.2. *Spatial Approximation*

A pseudospectral collocation–Chebyshev and Fourier method is implemented. In the meridional plane (r, z), each dependent variable is expanded in the approximation space P_{NM}, composed of Chebyshev polynomials of degrees less than or equal to N and M, respectively, in the r- and z-directions, while Fourier series are introduced in the azimuthal direction for the three-dimensional solution.

Thus, we have for each dependent variable f:

$$f_{NMK}(r, \phi, z, t) = \sum_{n=0}^{N} \sum_{m=0}^{M} \sum_{k=-K/2}^{K/2-1} \hat{f}_{nmk}(t)T_n(r)T_m(z)\exp(ik\phi) \qquad (3.2)$$

where T_n and T_m are Chebyshev polynomials of degrees n and m.

This approximation is applied at collocation points, where the differential equations are assumed to be satisfied exactly (Gottlieb & Orszag 1977; Canuto *et al.* 1987). We have considered the Chebyshev–Gauss–Lobatto points, $r_i = \cos(i\pi/N)$ for $i \in [0, N]$ and $z_j = \cos(j\pi/M)$ for $j \in [0, M]$, and a uniform distribution in the azimuthal direction: $\phi_k = 2k\pi/K$ for $k \in [0, K]$.

3.3. *Numerical approach*

For the axisymmetric regimes, the approach is based on an influence matrix technique introduced to treat the lack of boundary conditions for the vorticity (Chaouche *et al.* 1990). For the three-dimensional solution, the method is the one developed and described in Hugues (1998) (see also Hugues *et al.* 1998; Randriamampianina, Leonardi & Bontoux 1998). It is based on an efficient projection scheme to solve the coupling between the velocity and the pressure. This algorithm ensures a divergence-free velocity field at each timestep, maintains the order of accuracy of the time scheme for each dependent variable and does not require the use of staggered grids (Hugues & Randriamampianina 1998).

A complete diagonalization of operators yields simple matrix products for the solution of successive Helmholtz and Poisson equations at each timestep (Haldenwang *et al.* 1984). The computations of eigenvalues, eigenvectors and inversion of corresponding matrices are carried out once during a preprocessing step.

3.4. *Computational details*

The solution is assumed to be steady when the following criterion is satisfied by the approximation of the temporal derivative for each dependent variable f:

$$\mathrm{Err}(f) = \left| \frac{3f^{l+1} - 4f^l + f^{l-1}}{2\delta t} \right| < \epsilon, \tag{3.3}$$

where $\epsilon = 10^{-9}$ (close to machine zero).

For steady regimes, we have used $N \times M = 64 \times 48$ in the radial and axial directions with a timestep $\delta t = 0.1$ for $G > 0.3$, and $N \times M = 80 \times 48$ for $0.1 \leqslant G \leqslant 0.3$ with $\delta t = 0.05$. For higher values of the Reynolds number (unsteady regimes), the same grid is kept and different timesteps are considered within the numerical stability limit.

For the three-dimensional regimes, the same resolution as for the axisymmetric solutions is used in the meridional plane (r, z), while $K = 60$ Fourier modes in the azimuthal direction have been found to be sufficient to represent the wavy flows in all the cases studied here. Herrero *et al.* (1999) mentioned that an effective grid size of $n_c = 20$ nodes per wave cycle is required when performing fixed wavelength calculations. In the present study, the whole domain was taken into account in all of the computations carried out, as the number and size of waves change during the time integration.

4. The axisymmetric regimes

The Navier–Stokes equations admit to a unique solution for given initial conditions, unlike a stability analysis where different solutions may be observed, particularly the branches for the pitchfork bifurcation. In the present computations, no initial perturbation was imposed which could be varied, thus giving rise to a single solution. For the calculations of the different bifurcations, the strategy was to increase the value of the Reynolds number by a step of 25 until a significant change occurs in the flow. For the Hopf bifurcation points, this procedure was carried out until the value
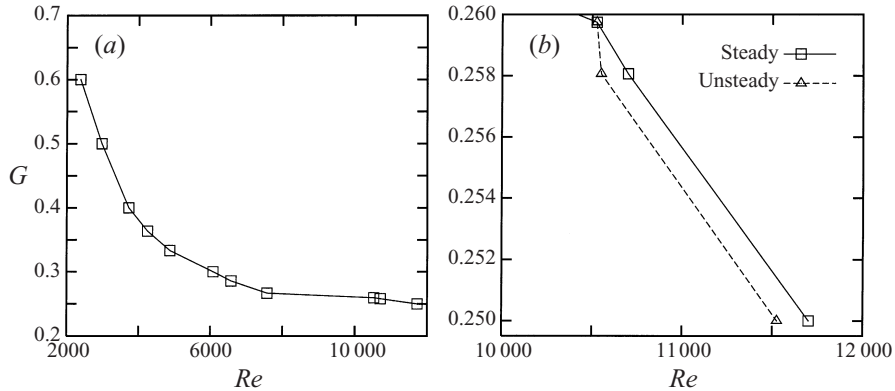
FIGURE 2. (a) Regime diagram for the pitchfork bifurcation, (b) detail for $G \leqslant G_c = 0.26$.

at which the criterion imposed for steady solution $\partial f / \partial t < 10^{-9}$ (see equation (3.3)) was not satisfied.

4.1. *The pitchfork bifurcation*

Iglesias & Humphrey (1998) observed a pitchfork bifurcation, characterized by a symmetry breaking with respect to the inter-disk midplane during axisymmetric steady computations at $7715 \leqslant Re \leqslant 23150$ for $G = 0.279$ and $R_c = 3.32$. This asymmetric solution was obtained after introducing a pertubation of 5% on the angular velocity of each disk (1.05Ω at the upper disk and 0.95Ω at the lower one). On the other hand, when relaxing the axisymmetry constraint ($\partial / \partial \phi \neq 0$), they reported transition to unsteady three-dimensional flow for $3700 < Re < 4440$, characterized by the presence of foci of intensified axial components of vorticity distributed periodically in the circumferential direction.

The regime diagram in the (Re, G)-plane obtained for the pitchfork bifurcation is displayed in figure 2. For $0.6 \geqslant G > 0.26$, the curve decreases rapidly with increasing rotation rate, followed by a saturation, corresponding to a very slow variation for $0.25 \leqslant G \leqslant 0.26$ (figure 2a). It was found that for $G \leqslant G_c \sim 0.26$, corresponding to $S = s/b = 0.13$, the flow first becomes unsteady, for a range of values of Re, before converging again to another steady state, but showing an asymmetrical structure with respect to the inter-disk midplane. This is shown in figure 2(b). In their transition diagram from axisymmetric to unsteady three-dimensional regimes in the plane (Re, S) for a curvature parameter $R_c = 3.32$, Herrero *et al.* (1999) found that there exists a critical value of $S \sim 0.13$ (corresponding to $G \sim 0.28$ for this curvature parameter) above which the flow evolves to a three-dimensional regime with symmetry breaking (regime III), and below which another three-dimensional regime with shift-and-reflect symmetry develops (regime II). For the latter, the authors mentioned that the axisymmetric solutions were already unsteady. Tavener *et al.* (1991) observed steady symmetry breaking in a similar configuration, but for larger values of the aspect ratio ($2 \leqslant G \leqslant 4$). They emphasized the important role played by the rotating hub in such geometries on the development of different bifurcations, and showed that this rotation triggers more rapidly the occurrence of asymmetric solutions compared with a stationary hub. Depending on the gap ratio, the onset of symmetry breaking may be smooth and reversible, or sudden with the presence of hysteresis. Such behaviour applies for the present study, according to the regime diagram displayed in figures 2(a) and 2(b), with smooth and reversible behaviour for $G > G_c$.
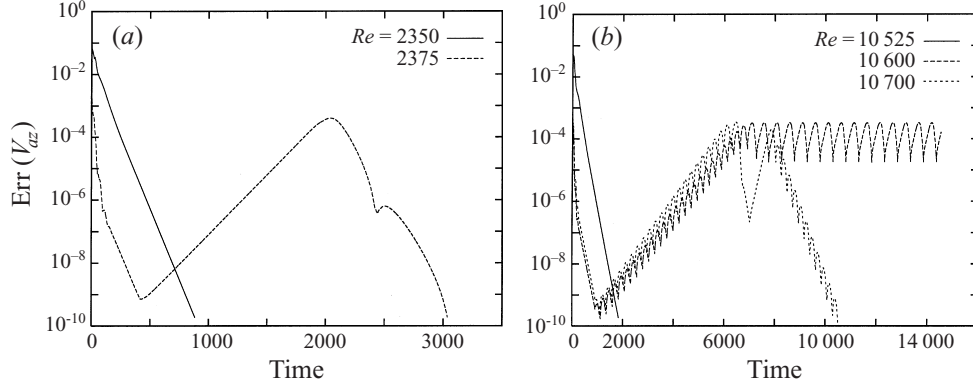
FIGURE 3. Convergence history of the azimuthal velocity during the pitchfork bifurcation for the two aspect ratios. (a) $G = 0.6$, (b) $G = 0.258$.

The characteristic jump of the tangential velocity within region II during the bifurcation to the steady symmetry breaking regime is found to decrease with the aspect ratio: at $G = 0.6$, $(V_{\phi/sym} - V_{\phi/asym})/V_{\phi/sym} \sim 3\%$, while at the lower gap ratio $G = 0.258$ it is about 0.3%. The results suggest that, when decreasing the aspect ratio, the onset of the symmetry breaking is delayed and eventually does not occur during the axisymmetric computations. It was not possible to capture this steady asymmetric structure for $G < 0.25$; the presence of hysteresis as reported by Tavener *et al.* (1991) may explain such behaviour. However, this phenomenon does develop for three-dimensional computations, and has been observed experimentally (Abrahamson *et al.* 1989).

The time history of the approximate temporal derivative of the tangential velocity component $Err(V_\phi)$ is shown in figure 3, at the value of Re at which the flow loses its symmetry with respect to the inter-disk midplane for $G = 0.6$ and 0.258. These curves reflect in more detail the bifurcation related to the jump mentioned above. The convergence behaviour at the lowest value of Re exhibiting a symmetrical solution is also reported in figure 3. For $G = 0.258$, following the exponential decrease, we remark on the 'oscillatory' behaviour of the time derivative which is sustained for $10\,525 < Re < 10\,700$ (see figure 2b), and is damped for $Re = 10\,700$ until the criterion in (3.3) is reached. We note particularly the time taken to reach the final steady solution for the two aspect ratios ($t \sim 3000$ for $G = 0.6$ and $t \sim 10^4$ for $G = 0.258$) as well as the duration of the first stage during which the flow keeps a perfect symmetry with respect to the inter-disk midplane. These results may be compared with the solution reported by Iglesias & Humphrey (1998) with $G = 0.279$.

4.2. *The Hopf bifurcation*

The regime diagram for the Hopf bifurcation is shown in figure 4, giving the critical value of the gap ratio versus the critical Reynolds number at the transition to unsteadiness. We note two distinct behaviours, for $0.26 < G \leqslant 0.6$ and for $0.1 \leqslant G \leqslant 0.26$, which are related to the pitchfork bifurcation (also shown in the same figure). For $G \leqslant G_c = 0.26$, we did not take into account the range of Reynolds numbers where the flow is already time-dependent, but the computations have been started from the steady asymmetric solutions. For the two bifurcations, the critical gap ratio varies approximately with Re^{-1} for $G > G_c$, with a steeper slope occurring
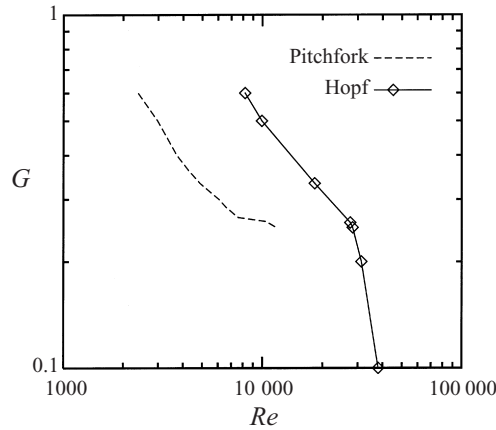
FIGURE 4. Regime diagram for the pitchfork and Hopf bifurcations.

for the lower values of G. The oscillatory motion results from the flapping inward flow from the casing in region II meeting the detached shear layer (region III) which acts like a compliant surface (see Schuler *et al.* 1990; Humphrey & Gor 1993). Such a phenomenon can be related to the Coanda effect (see Tritton 1988, chapter 12).

5. The three-dimensional regimes

The three-dimensional solution is obtained by integrating the momentum equations, using the axisymmetric solution as the initial condition into which a finite perturbation is introduced for the tangential velocity in each azimuthal plane. In the present case, this initial solution corresponds to:

$$V_{\phi,3d} = V_{\phi,axi}(1 + \alpha \sin(m\phi)), \tag{5.1}$$

where α is the amplitude of the perturbation (fixed at 0.10), and m is an integer.

One major difficulty arising from the numerical studies of wave problems in rotating systems comes from the intransitivity of the flow, corresponding to the coexistence of different solutions obtained from the same physical (boundary) conditions (Fowlis & Hide 1965; Hignett *et al.* 1985; Abrahamson *et al.* 1989).

Following the above study of axisymmetric flow regimes, we have considered two aspect ratios: $G = 0.6$ and 0.258, for which different behaviour was observed during the pitchfork bifurcation. A detailed study of the transition from axisymmetric to three-dimensional solutions is carried out for the larger aspect ratio. For $G = 0.258$, we have taken a value of the rotation rate ($Re = 10\,600$) lying within the small region between the two steady regimes (symmetric and asymmetric with respect to the inter-disk midplane), at which the flow is unsteady (see figures 2*b* and 3).

5.1. $G = 0.6$: *transition to the unsteady three-dimensional regime*

Transition to the unsteady three-dimensional regime was obtained for $3350 < Re \leqslant 3750$. This corresponds to a value of $1005 < Re_H \equiv 2ReG/(R_c + 1) \leqslant 1125$, which is far from the value $Re_H \sim 2049$ found by Iglesias & Humphrey (1998) for $R_c = 3.32$ and $G \leqslant 0.279$ (see also Humphrey & Gor 1993). This large discrepancy suggests that the gap-ratio-related Re_H criterion is insufficient to delineate this transition.

During the present computations, the indeterminate regime observed by Abrahamson *et al.* (1989) for $G \leqslant 0.2$ was not found, but the flow entered directly the

Re	m	λ_{II}	f	f'	δ_{II}/b	δ_{III}/b	Ω_I/Ω	Ω_{II}/Ω	Ω_{III}/Ω
3750	3	$\pi/3$	1.39×10^{-2}	2.476×10^{-4}					
3750	8	$\pi/4$	1.695×10^{-2}		0.145	0.075	0.075	0.697	0.867
4250	3	$\pi/3$	1.383×10^{-2}						
5000	3	$\pi/3$	1.381×10^{-2}						
10^4	5	$2\pi/5$	1.129×10^{-2}	6.1×10^{-4}					

TABLE 1. Summary of three-dimensional results for $G = 0.6$, with m the initial perturbation, λ the circumferential wavelength, f the frequency, δ the radial extent.

alternating vortex states regime, characterized by the occurrence of multiple solutions with the existence of a predominant state. Such a phenomenon can be obtained from numerical studies by imposing different initial perturbations (see Hignett *et al.* 1985). We have considered three different values for the wavenumber for the perturbation applied to the axisymmetric solution used to generate the three-dimensional flow in (5.1): $m = 3$, 7 and 8. At $Re = 3750$, with an initial wavenumber $m = 3$, the final solution exhibits a temporal quasi-periodic regime, characterized by two incommensurate frequencies with a fundamental f and a second f' given in table 1. With $m = 7$, a quasi-periodic motion is still obtained. With an initial value of $m = 8$, a monoperiodic flow is established, rapidly in comparison with the two previous solutions where a long chaotic transient is observed. Indeed, all the numerical works related to the present configuration have reported a monoperiodic behaviour of the three-dimensional solution at the transition from the axisymmetric solution, but no quasi-periodic motion (see Iglesias & Humphrey 1998; Herrero *et al.* 1999).

Similarly to the successive pairing mentioned in Abrahamson *et al.* (1989) during their indeterminate regime, we have also observed such significant changes during the chaotic transient for the '$m = 3$' solution. The temporal evolution of the modulus of the dimensionless vorticity at fixed isovalues is displayed in figure 5 at different (r, ϕ)-planes, at midheight $z/s = 0.50$. We consider first the shape of the polygonal boundary for the inner region, mentioned by Abrahamson *et al.* (1989) to result from the presence of the vortices in the outer region. The number of vortices, hence the number of sides of the polygon, reduces with time during the transient, beginning at nine and finally stabilizing at six. At the time where the final solution establishes (figure 5f), the flow structure is well defined by six vortices around a hexagon, giving a circumferential wavelength $\lambda = \pi/3$ and showing symmetry with respect to $\phi = \pi$. The small difference in the size of the vortices results from the second frequency (two orders of magnitude smaller than the fundamental). Pairing of vortices can be identified clearly from isocontours during the transient stage until figure 5(e) (note its time duration $t \sim 1400$). Although the geometrical configurations are completely different, very similar behaviour can be observed from the different phases reported by van de Konijnenberg *et al.* (1999) during the establishment of a final wavy solution in a rotating tank.

5.2. $G = 0.6$: the '$m = 8$' solution

Humphrey, Schuler & Webster (1995) found from their numerical studies (with $G = 0.196$) that the circumferential wavelength of the vortices for the axial velocity is twice that of the radial and tangential velocity components at midheight of the cavity. They found that at the inter-disk midplane, 'the axial component of vorticity manifests itself as an even number of circumferentially periodic foci'. However, Abrahamson *et*
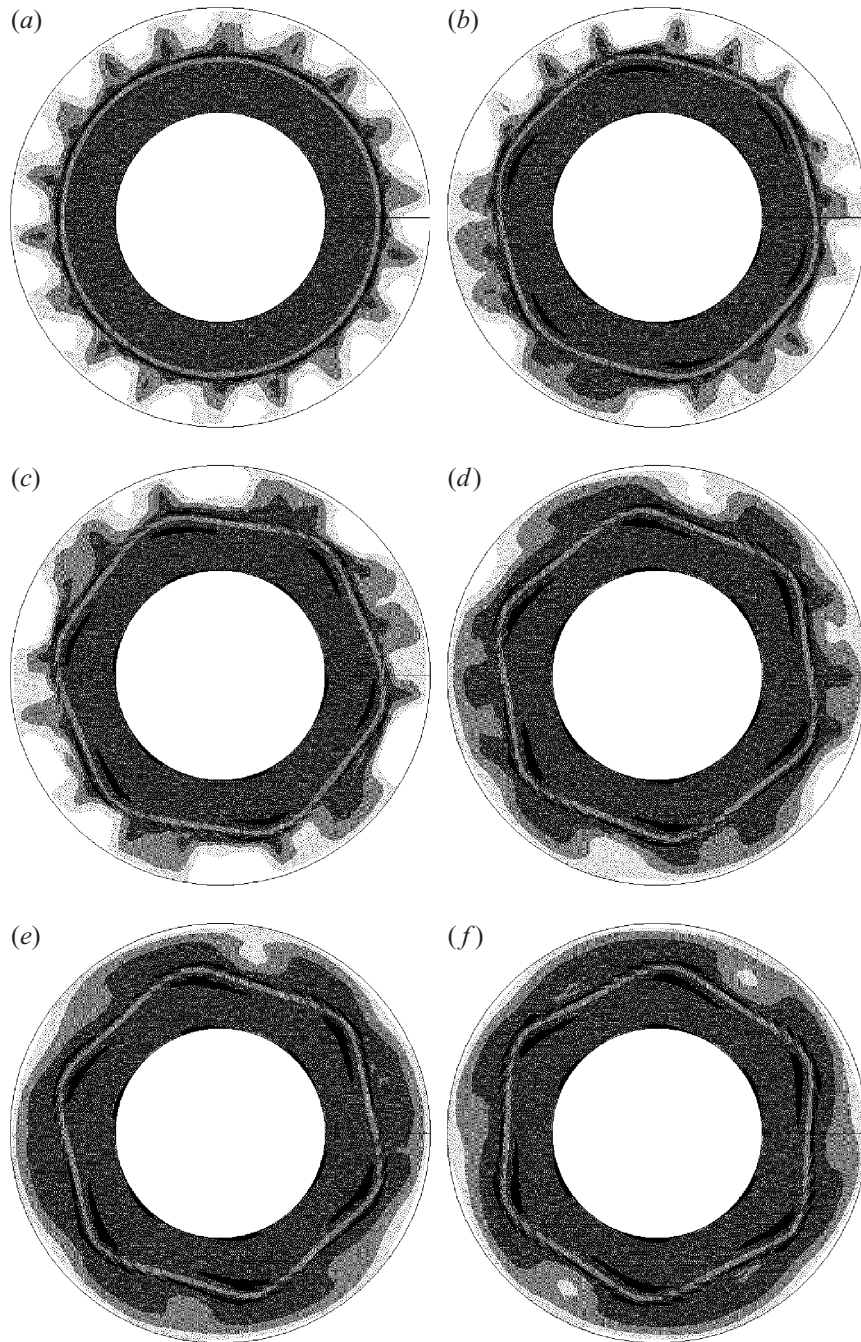
FIGURE 5. Temporal evolution of the distributions of the modulus of the dimensionless vorticity field in the (r, ϕ)-plane for $G = 0.6$ and $Re = 3750$ at $z/s = 0.50$ (five levels with $0 \leqslant |\zeta| \leqslant 1.12$): (a) $t = 327.40$; (b) $t = 734.40$; (c) $t = 936.7125$; (d) $t = 1345.525$; (e) $t = 1409.3375$; (f) $t = 1816.2125$. Resolution: $N \times M \times K = 64 \times 48 \times 60$, timestep $\delta t = 0.0625$.
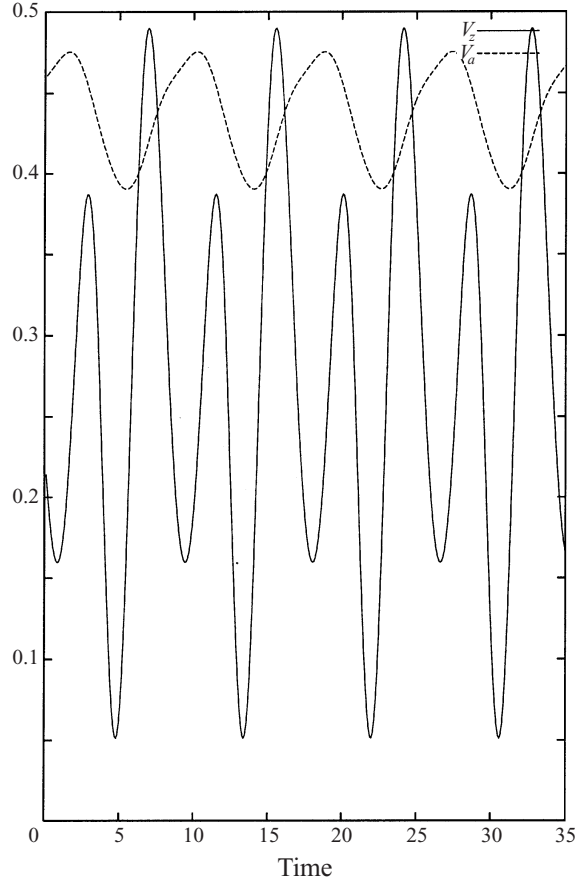
FIGURE 6. Temporal evolution of the axial V_z and tangential $Va \equiv V_\phi$ velocity components at a monitoring point for the '$m = 8$' solution: $G = 0.6$, $Re = 3750$ (to have the same level on the two evolutions, the axial velocity component is fictitiously magnified by a factor 20 in the figure).

al. (1989) visualized an odd number of vortices for a value of the gap ratio close to that studied by Humphrey *et al.* (1995), and 7 vortices were obtained from the present computations. Humphrey *et al.* (1995) also mentioned that the frequency of the oscillations in the axial direction is twice that of the radial and azimuthal directions, and that a linear correlation links the frequency to the wavelength (see also Herrero *et al.* 1999). Similar behaviour is also observed during the present computations, as shown by the temporal evolution of the tangential and axial velocity components at the same monitoring point located in region II (figure 6). The two components oscillate with the same fundamental frequency f, but the axial component shows clearly a period doubling with $\frac{1}{2}f_w \equiv \frac{1}{2}f$. The flow is composed of stable structures, and this result is related to the spatial behaviour of the axial velocity, emphasizing the strong nonlinearity of the motion. The perturbation fields of the azimuthal and axial velocity components, displayed in the (r, ϕ)-plane in figure 7 at three different heights, $z/s = 0.34$, 0.50 and 0.66, are consistent with such findings. The radial and tangential velocities show identical behaviour. At $z/s = 0.5$, the azimuthal wavelength of the radial and tangential velocity components in the outer region is $\lambda_u = \lambda_v = 2\pi/16$, while for the axial component it corresponds to $\lambda_w = 2\pi/8 \equiv 2\lambda_u = 2\lambda_v$. The latter

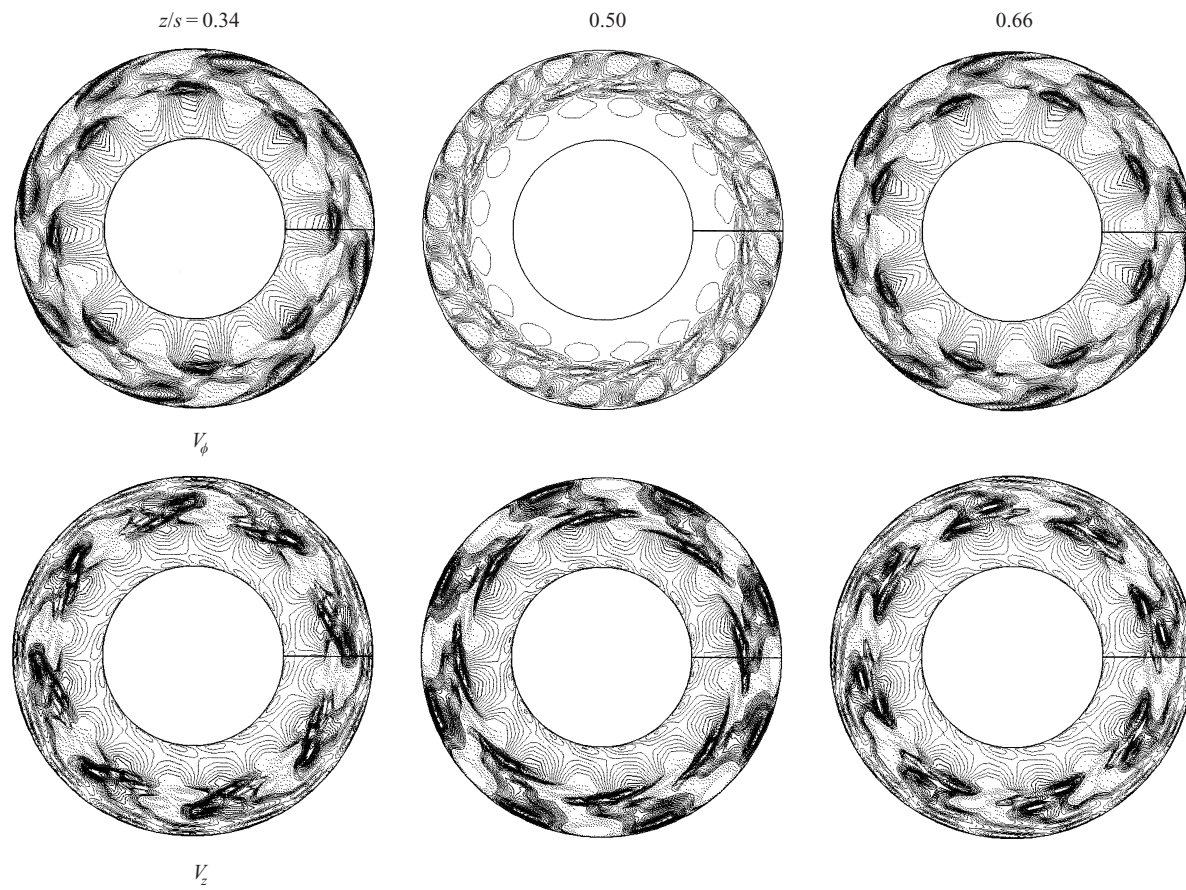$z/s = 0.34$ 0.50 0.66

V_ϕ

V_z

FIGURE 7. Variation of the instantaneous perturbation fields of dimensionless azimuthal V_ϕ and axial V_z velocity components at different (r, ϕ)-planes for $Re = 3750$ for the '$m = 8$' solution (52 levels with $-0.085 \leqslant V_\phi \leqslant 0.086$ and $-0.064 \leqslant V_z \leqslant 0.064$).
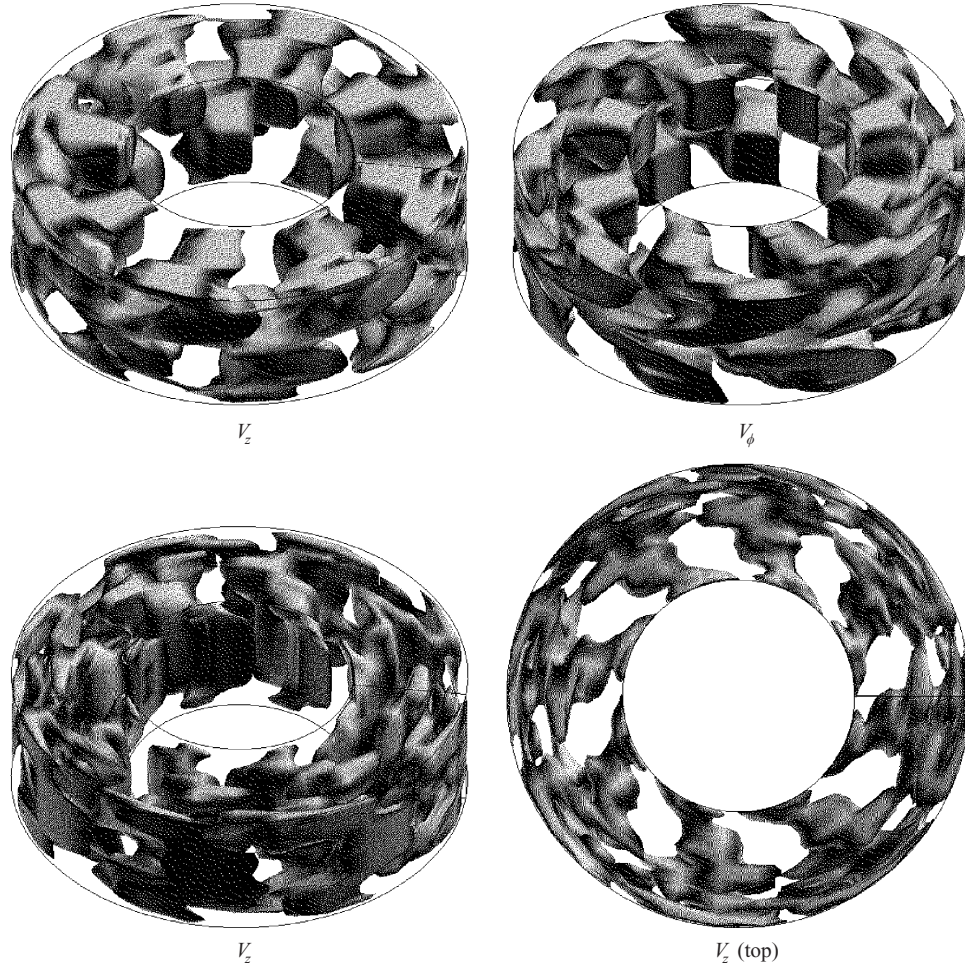
V_z V_ϕ

V_z V_z (top)

FIGURE 8. Instantaneous iso-surface of the perturbation of the dimensionless velocity components for $G = 0.6$ and $Re = 3750$ for the '$m = 8$' solution.

value of λ_w is independent of the height considered while $\lambda_u = \lambda_v = 2\pi/8 \equiv \lambda_w$ at the other heights. The corresponding wavelength in the inner region for the tangential and axial components remains at the same value for all the heights $(2\pi/8)$. From the isovalues of the radial component, a shift-and-reflect symmetry with respect to the midheight is observed, which generates twice the number of vortices at $z/s = 0.5$ than at other heights, while the axial component exhibits the antisymmetry required to ensure mass conservation. The shroud boundary layer contains eight pairs of elongated contrarotating vortices, especially visible from the axial velocity component at the midheight (figure 7). Abrahamson *et al.* (1989) observed that this region has a more three-dimensional nature than the inner and core regions.

The strong exchanges between the three regions are visible from the iso-surfaces of the three velocity components, presented in figure 8 from the same viewpoint (with a view from the top in the (r, ϕ)-plane of the axial component). It is clearly seen that the flow is composed of eight vortices. For the radial and tangential components, these are disposed symmetrically with a shift with respect to the midheight as already observed from the isocontours, while for the axial component they are formed by
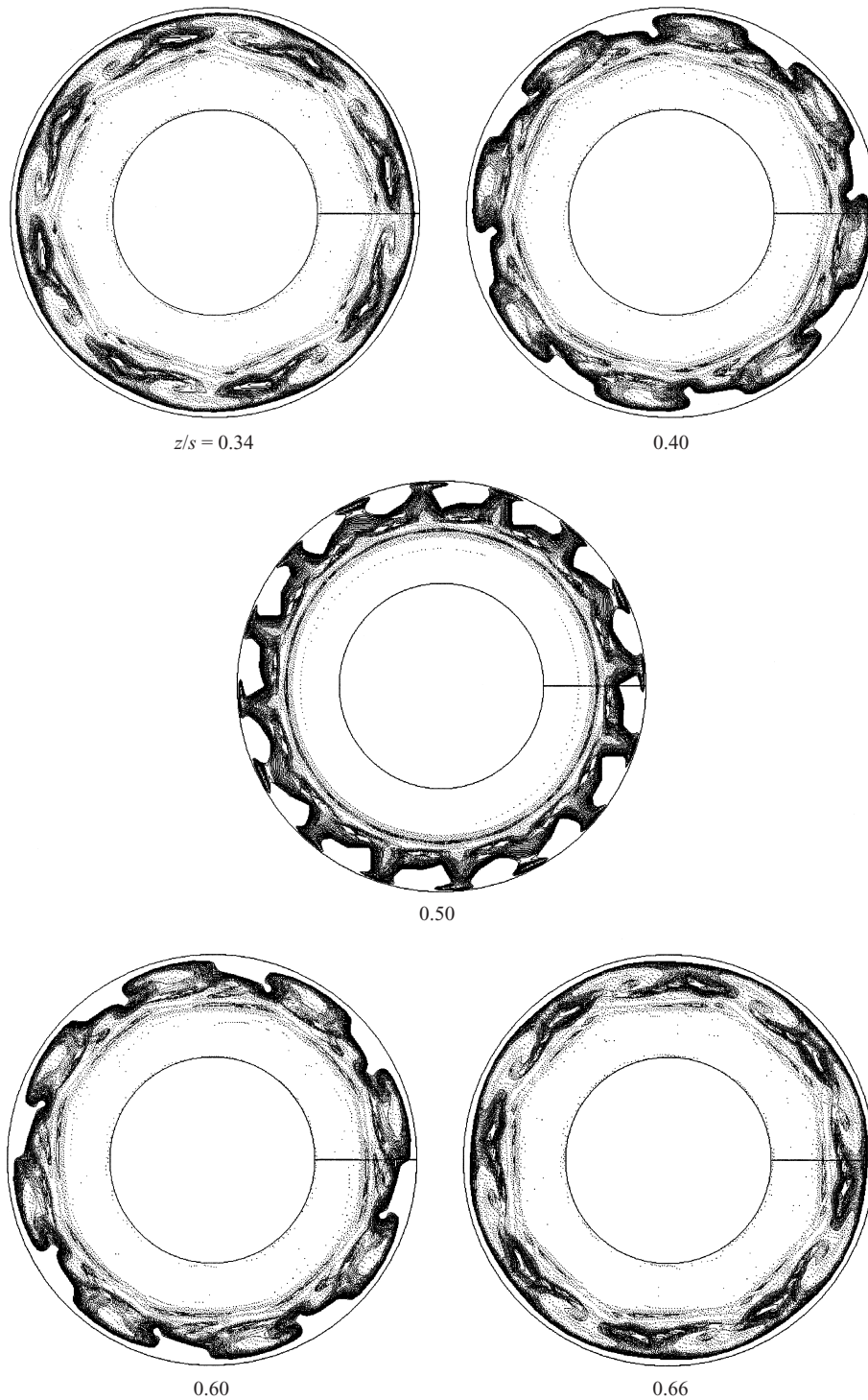
$z/s = 0.34$ 0.40

0.50

0.60   0.66

FIGURE 9. Instantaneous distributions of the modulus of the vorticity at five (r, ϕ)-planes for the '$m = 8$' solution: $G = 0.6$ and $Re = 3750$ (52 levels with $0 \leqslant |\zeta| \leqslant 1.14$).
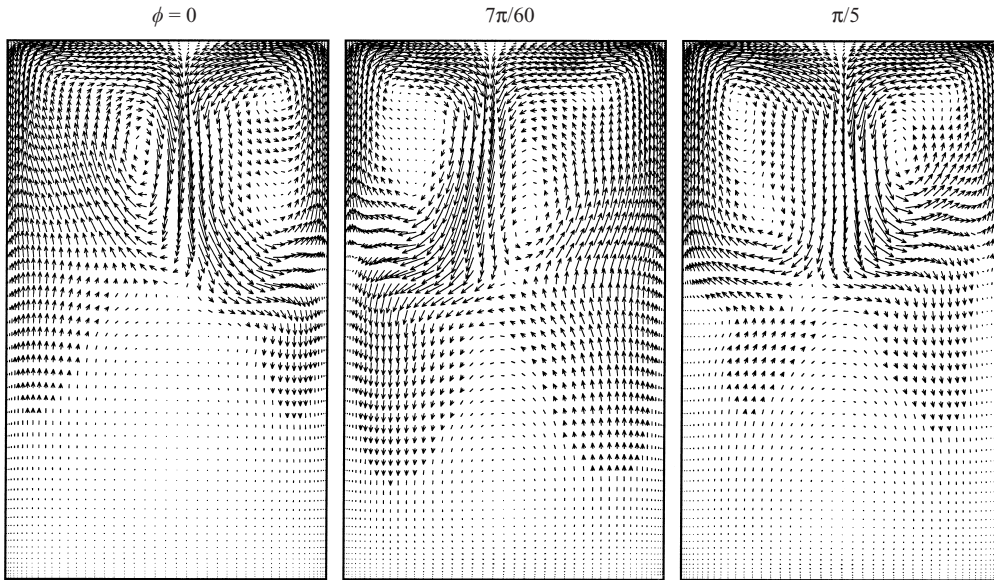
FIGURE 10. Instantaneous velocity vectors at different (r, z)-planes for $G = 0.6$ and $Re = 3750$ for the '$m = 8$' solution (vectors obtained using the axial and radial components only).

eight twisted structures. The instabilities in the radial component are oriented in an opposite sense to those for the two other components. Such an arrangement explains the presence of twice the number of vortices at the inter-disk midplane than at other heights. The elongated toroidal vortices in the shroud boundary layer are particularly visible on the iso-surface of the axial component. The exchange between the outer and inner regions appears to develop through spiral arms, as reported by Akhmetov & Tarasov (1987). The spiral arms form a negative angle with respect to the tangential direction which varies with radius (see figure 8). This so-called type II instability has been reported in the literature (with respect to the stability of Ekman layers in rotating cavities) to result from the effect of centrifugal and Coriolis forces. The spiral form of these exchanges is due to the different angular velocities between the different regions, as the shroud is fixed while the hub rotates with the disks.

The distribution of the modulus of the vorticity is displayed in figure 9 at different (r, ϕ)-planes to emphasize the nature of the flow regime. An eight-sided boundary (corresponding to the detached shear layer) separates the inner and outer regions at symmetrical heights with the exception of the midheight. Eight pairs of large contrarotating vortices are clearly visible in the outer region, with smaller ones near the edge of the inner region. At the inter-disk midplane, there are 16 small structures of differing sizes in the outer region. This results from the 'pairing' of the vortices developing at the other heights for $0.40 \leqslant z/s \leqslant 0.60$ as seen in the figure, with a wavelength $\lambda = 2\pi/4$ for this whole width. As mentioned above, this behaviour is due to the different arrangement of the velocity components. At other heights, we observe a wavelength $\lambda = 2\pi/8$, with reflection of structures about the inter-disk midplane, and with a lag corresponding to $\frac{1}{2}\lambda = \frac{1}{8}\pi$ (see the figure at $z/s = 0.34$ and 0.66). It is noteworthy that such a shift-and-reflect symmetry is also visible at other heights, although the value of the wavelength changes (see the figure at $z/s = 0.40$ and 0.60). These structures are in agreement with the definition of regime II given by Herrero *et al.* (1999). The velocity vectors displayed at different (r, z)-planes in figure

10 emphasize the shift-and-reflect behaviour of the solution. Although the centres of the two recirculating cross-stream flows in the outer region show a shift with respect to the inter-disk midplane, a symmetry breaking is not clearly observed. Note the exchange between the inner and outer regions, following the recirculations mentioned above. A symmetry reflection with respect to $\frac{1}{4}\pi$ is also obtained for these fields.

5.3. *G = 0.6: the effect of rotation rate*

The effect of the rotation rate on the solution is studied by increasing the Reynolds number up to $Re = 10^4$, at which the corresponding axisymmetric solution is already unsteady (see figure 4). As for the computations described above at $Re = 3750$, the strategy was to test different initial wavenumbers on the axisymmetric solution leading to the 'most stable' three-dimensional flow.

Characteristics of the results obtained for $Re = 4250$, 5000 and 10^4 are summarized in table 1. An initial perturbation with $m = 3$ generates a monoperiodic behaviour for $Re = 4250$ and 5000, while a quasi-periodic motion establishes for $Re = 10^4$ with $m = 5$. Isocontours of the axial velocity component at different (r, ϕ)-planes are shown in figure 11. For the monoperiodic solutions, the final flow structure shows six vortices of equal size in the (r, ϕ)-plane, giving a circumferential wavelength $\lambda = \frac{1}{3}\pi$, with a complete symmetry with respect to the inter-disk midplane. Higher rotation rate results in a more twisted zone at the limit of the inner region, and consequently more intense exchange between the two regions. The two solutions correspond to the shift-and-reflect symmetry regimes reported by Herrero *et al.* (1999), but also with the presence of a hexagonal zone separating the inner and outer regions. At $Re = 10^4$ the flow structure is composed of five vortices of similar sizes, with small differences resulting from the quasi-periodic nature of the flow. The shift-and-reflect symmetry no longer appears, and a symmetry breaking starts to develop, as shown by the velocity vectors at different (r, z)-planes (figure 12). The findings are consistent with those of Herrero *et al.* (1999) when increasing the rotation rate. The inner region is no longer in solid-body rotation, with the presence of small vortices, in agreement with the observations of Abrahamson *et al.* (1989). The structures displayed at two planes separated by π, respectively, at $\phi = 3\pi/10$ and $13\pi/10$ show no hint of symmetry.

5.4. *Small gap ratio: G = 0.258*

The rotation rate $Re = 10\,600$ is chosen here, for which the corresponding axisymmetric solution is already unsteady (see figures 2*b* and 3). An initial wavenumber $m = 3$ in (5.1) triggers a quasi-periodic solution. Different flow structures develop compared with those observed at the larger gap ratio $G = 0.6$. The flow structure contains six vortices, as seen from the isocontours of the modulus of the dimensionless vorticity at different (r, ϕ)-planes (figure 13) displayed at the final time considered, more visible from the spiral arms in the inner region. However, a spatial periodicity of $\lambda = 2\pi/3$ is observed, instead of $\pi/3$, resulting from the quasi-periodic nature of the flow as mentioned above.

The shift-and-reflect symmetry expected for this case according to the regime diagram produced by Herrero *et al.* (1999) is not obtained, as shown by the isovalues of vorticity at $z/s = 0.34$ and 0.66 (figure 13). This discrepancy may result from the different values of the curvature parameter, as well as from differences in the numerical approaches considered. The outer region is shifted towards the boundary layer on the casing, and strong exchanges with the inner region develop in the upper half of the cavity via spiral arms. Each spiral arm is indeed associated with a vortex located in the outer region. Elongated vortices develop in the inner region, located near the
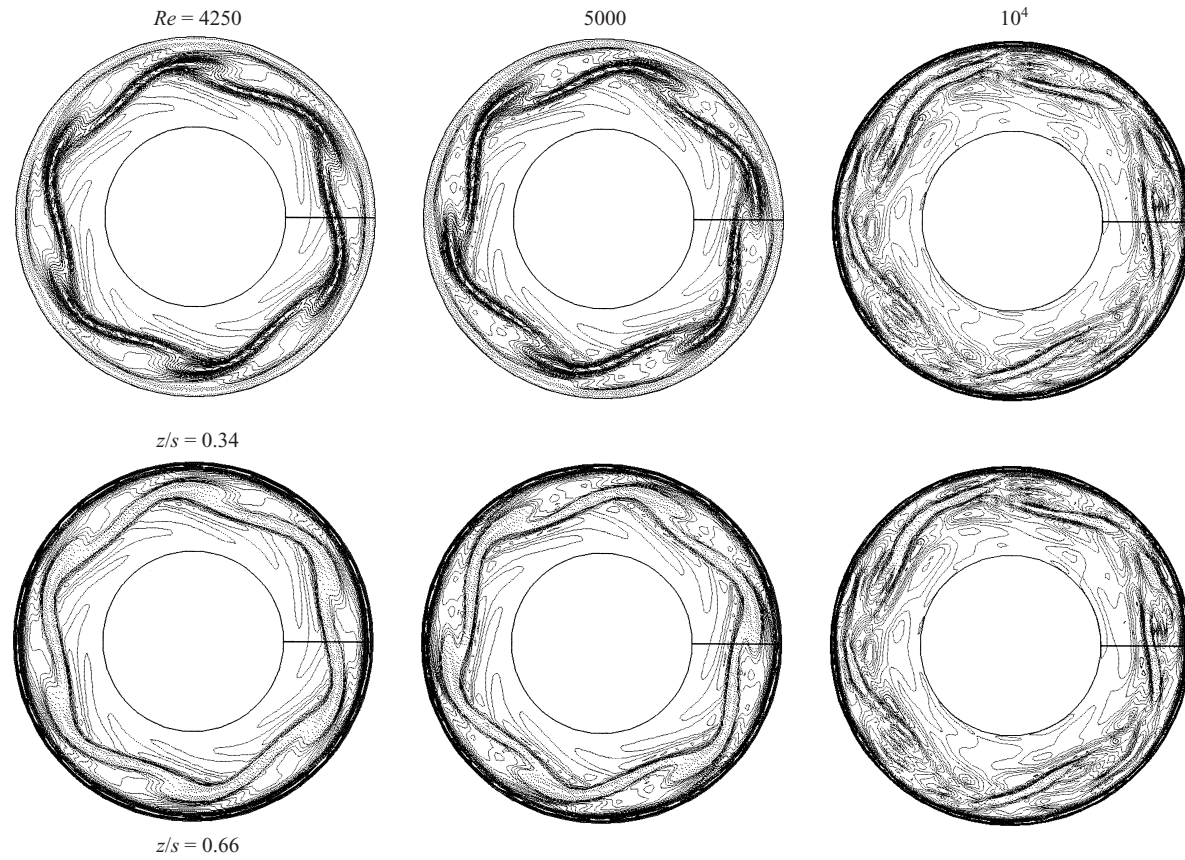
Re = 4250   5000   10^4

z/s = 0.34

z/s = 0.66

FIGURE 11. Effect of the rotation rate on the instantaneous isocontours of the dimensionless axial velocity component at two (r, ϕ)-planes (52 levels with $-0.159\,58 \leqslant V_z \leqslant 0.159\,58$ for $Re = 4250$, $-0.163\,29 \leqslant V_z \leqslant 0.163\,29$ for $Re = 5000$ and $-0.177\,492 \leqslant V_z \leqslant 0.180\,504$ for $Re = 10^4$).

$$\phi = 3\pi/10 \qquad\qquad 7\pi/10$$

$$9\pi/10 \qquad\qquad 13\pi/10$$

FIGURE 12. Velocity vectors at different (r, z)-planes for $G = 0.6$ and $Re = 10^4$ with an initial perturbation $m = 5$ (vectors obtained using the axial and radial components only).

boundary between the outer and inner regions. However, the casing boundary layer shows a more axisymmetrical structure, and does not exhibit the toroidal structure observed for $G = 0.6$ at $Re = 3750$. The flow structure in the (r, z)-planes presents a more pronounced symmetry breaking with respect to the inter-disk midplane than that obtained from axisymmetric computations, with a disctinct primary dominant
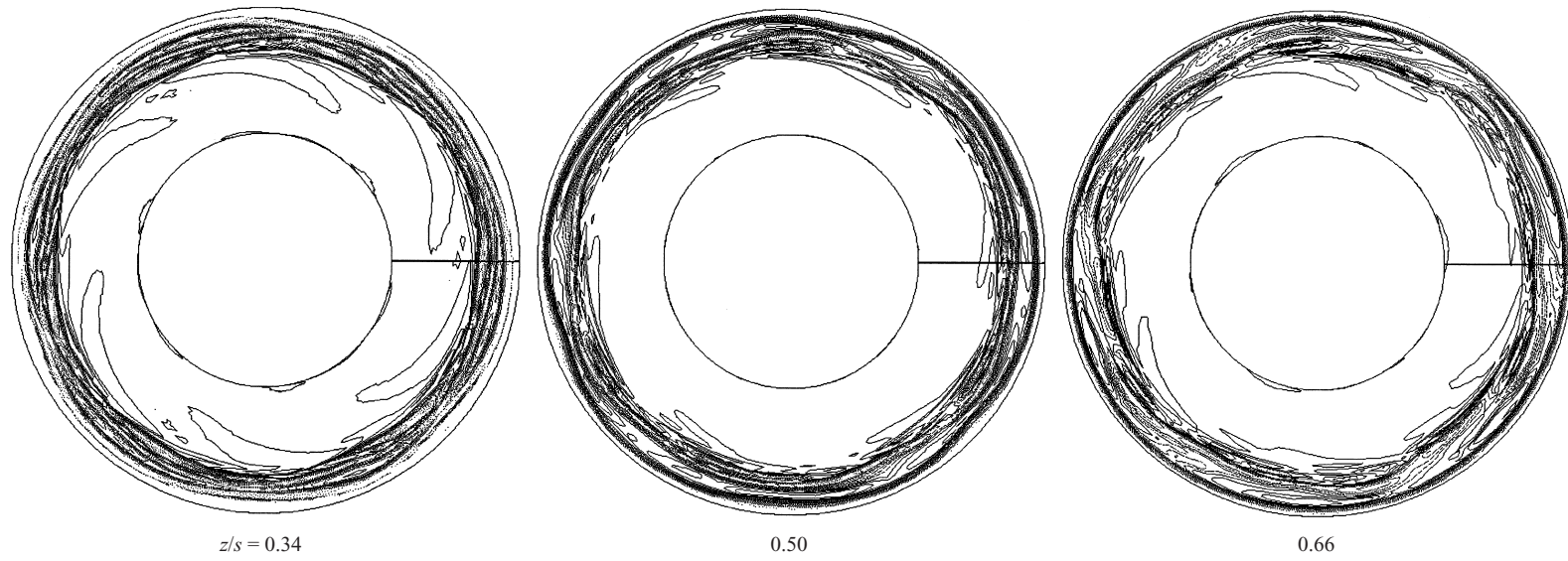
z/s = 0.34 0.50 0.66

FIGURE 13. Distributions of the modulus of the dimensionless vorticity field at different (r, ϕ)-planes for $G = 0.258$ and $Re = 10\,600$ (32 levels with $0 \leqslant |\zeta| \leqslant 1.2$).
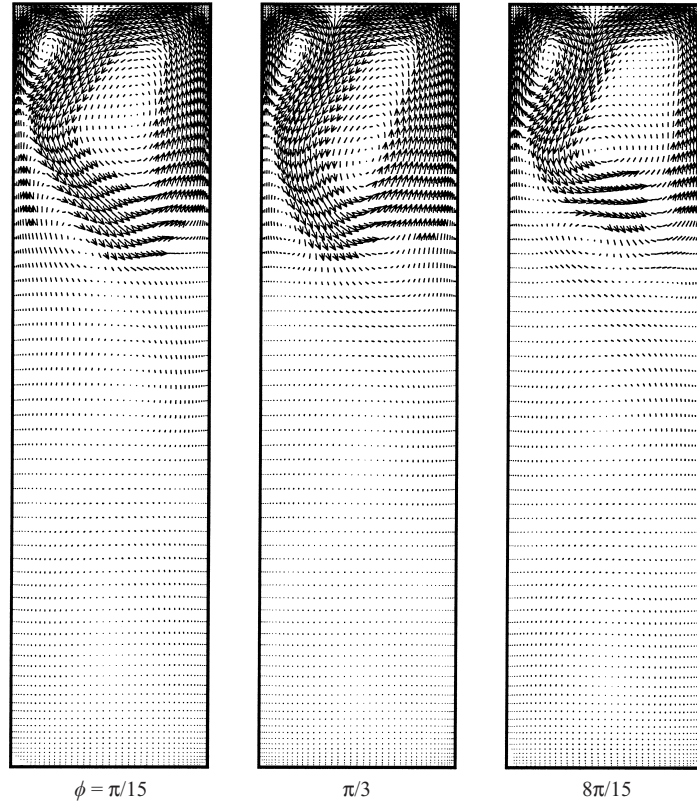
$$\phi = \pi/15 \qquad\qquad \pi/3 \qquad\qquad 8\pi/15$$

FIGURE 14. Instantaneous velocity vectors at different (r, z)-planes for $G = 0.258$ at $Re = 10\,600$.

vortex (figure 14). The shift of the centre of this primary cell at different (r, z)-planes is associated with the presence of a tertiary cell located just below it, in the region of the flow responsible for the unsteadiness. From these observations, it is concluded that the present solution belongs to regime III as reported by Herrero *et al.* (1999), although the polygonal shape of region III is not clearly distinguishable.

6. Discussion

The three-dimensional results are summarized in table 1 for $G = 0.6$ and in table 2 for $G = 0.258$.

Owen & Rogers (1995) described the occurrence of Rankine vortex behaviour in some rotating cavity flows, characterized by the following variation of $V_\phi/\Omega r$ with $x^{-2} = (r/b)^{-2}$:

$$V_\phi/\Omega r = Ax^{-2} + B, \qquad (6.1)$$

where A and B are two constants. Gan *et al.* (1996) identified this behaviour in their ECDP measurements for $G = 0.6$ at large values of Re. The variation of the ensemble-averaged normalized tangential velocity $V_\phi/\Omega r$ for the two aspect ratios studied here is shown in this form in figure 15. Time-averaged results for the axisymmetric solution are also shown. These results show the different characteristics of each region, with a larger extent of the inner region and a smaller outer region for the larger aspect ratio, as described above. Rankine vortex behaviour is clearly observed in the outer
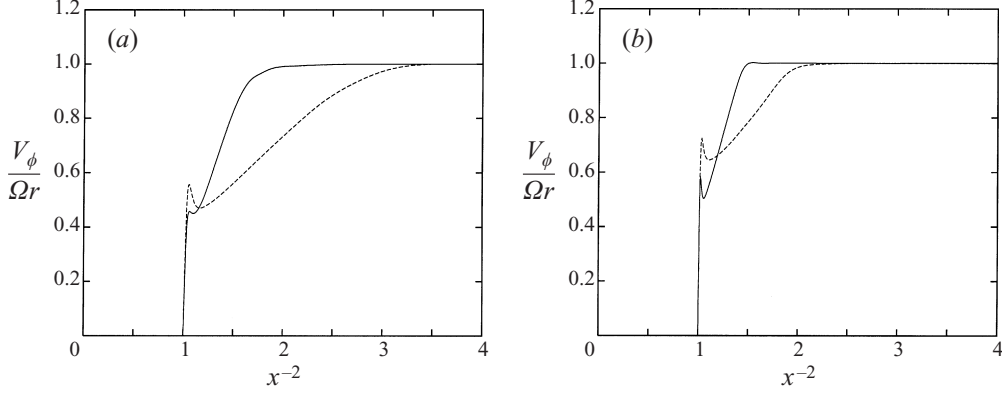
FIGURE 15. Variation of the normalized tangential velocity component $V_\phi/\Omega r$ with $x^{-2} = (r/b)^{-2}$ at $z/s = 0.80$: (a) $G = 0.6$ at $Re = 3750$ ($m = 8$); (b) $G = 0.258$ at $Re = 10\,600$ ($m = 3$). —, three-dimensional; $\cdots$, axisymmetric.

m	λ_{II}	f	f'	δ_{II}/b	δ_{III}/b	Ω_I/Ω	Ω_{II}/Ω	Ω_{III}/Ω
3	$2\pi/3$	1.1324×10^{-2}	7.72×10^{-4}	0.12	0.03	0.22	0.6455	0.916

TABLE 2. Summary of three-dimensional results for $G = 0.258$ and $Re = 10\,600$, with m the initial perturbation, λ the circumferential wavelength, f the frequency, δ the radial extent.

region, with a value of $B \sim 0$ for the axisymmetric solutions (see also Lewis *et al.* 1998), while $B \sim -1$ for the three-dimensional solutions.

The inner region behaves as a solid body, while the boundary layer along the casing has a different angular velocity (Ω_I/Ω) and the core region an angular velocity (Ω_{II}/Ω) depending on the gap ratio and rotation rate considered (see tables 1 and 2). Humphrey *et al.* (1995) proposed a theoretical value $\Omega_{II}/\Omega = 0.5$ at higher rotation rates for a gap ratio $G = 0.279$. Abrahamson *et al.* (1989) reported a larger value of about 0.8 from their experiments.

For region III, we obtained (Ω_{III}/Ω) = 0.867 for $G = 0.6$ at $Re = 3750$ (table 1). This is very close to the theoretical value predicted from the relation mentioned in Akhmetov & Tarasov (1987) for plane flow with polygonal regions of constant vorticity 2Ω:

$$\Omega_{III}/\Omega = (k-1)/k, \tag{6.2}$$

giving (Ω_{III}/Ω) = 0.875, where k is the number of corners of the polygon.

Humphrey & Gor (1993) provided an empirical variation for the radial extent and thickness of the detached shear layer:

$$r_{III}/b = 21.7(Re_H)^{-1.03} + 0.72, \tag{6.3}$$

and

$$\delta_{III}/b \sim (2Re)^{-1/2}, \tag{6.4}$$

where $Re_H = \Omega bs/\nu$. Use of the relation (6.3) for $G = 0.6$ at the corresponding $Re_H = 1125$ leads to $r_{III}/b = 0.7356$, which is close to the theoretical value 0.74 reported by Humphrey & Gor (1993) but smaller than the computed value: $0.835 > r_{III}/b \geqslant 0.76$. For the thickness, we obtain $\delta_{III}/b = 0.075$, which is close to the value measured by
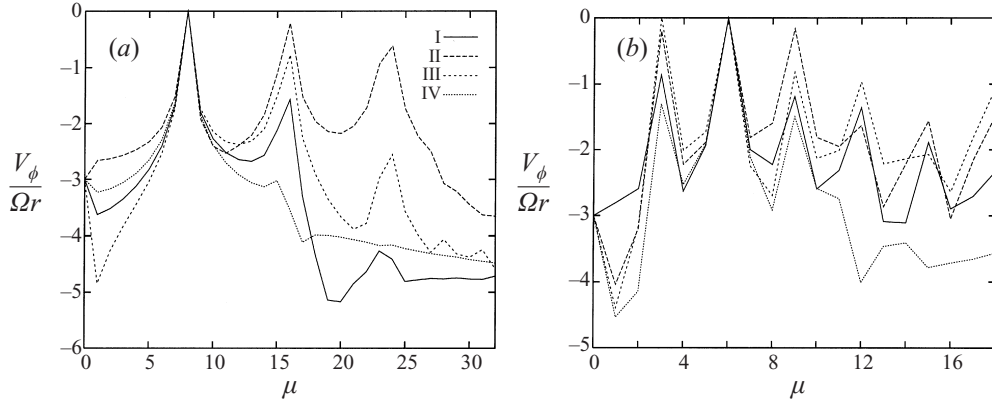
FIGURE 16. Spectral analysis of the spatial variation of the normalized tangential velocity component $V_\phi/\Omega r$ with wavenumber μ in the different regions of the flow: (a) $G = 0.6$ at $Re = 3750$ ($m = 8$); (b) $G = 0.258$ at $Re = 10\,600$ ($m = 3$).

Humphrey & Gor (1993) at $Re = 4065$ for $G = 0.293$, while the theoretical value from (6.4) gives $\delta_{III}/b = 0.107$. These discrepancies may result mainly from the difference on the curvature parameters considered: $R_c = 3.32$ in Humphrey & Gor (1993) while in the present configuration $R_c = 3$. Indeed, this parameter plays an important role on the flow behaviour, particularly on the transition to unsteadiness (see Daube *et al.* 1994).

The tangential velocity also possesses a spatial periodic nature in the (r, ϕ)-plane. The spectral analysis of this spatial variation of the tangential velocity with wavenumber $\mu = 2\pi/\lambda$ is reported in figure 16 for the different regions of the flow. Note the high density of the harmonics in region II (the outer region), showing the strong nonlinearity of the flow for both gap ratios. For $G = 0.6$, a wavelength of $2\pi/8$ is obtained for all the regions of the flow, as was observed directly from the flow structure. For $G = 0.258$, there is a spatial period doubling, with a density similar to the fundamental one in region III. The latter indicates that a wavelength $\lambda = 2\pi/3$ dominates for this configuration, although $\lambda = 2\pi/6$ is present within the flow. This behaviour emphasizes the complexity of the quasi-periodic motion of the flow mentioned above.

7. Torque coefficient C_m

The variation of the disk moment coefficient C_m versus rotational Reynolds number Re is displayed in figure 17 for $G = 0.6$. The value taken for time-dependent regimes has been obtained from a time-averaged velocity.

$$\tfrac{1}{2}\rho\Omega^2 b^5 C_m = \int_0^{2\pi}\int_a^b \mu\frac{\partial V_\phi}{\partial z}\bigg|_{z=0} r\,\mathrm{d}A + \int_0^{2\pi}\int_a^b \mu\frac{\partial V_\phi}{\partial z}\bigg|_{z=s} r\,\mathrm{d}A, \qquad (7.1)$$

where A is the area. The three-dimensional results give the same variation for the torque coefficient as the axisymmetric solutions, with $C_m \propto Re^{-n}$ where $n = 0.63$. Herrero *et al.* (1995) obtained a 'Reynolds number power dependency changing from -0.67 to -0.53 with increasing Re' for an aspect ratio $G = 0.196$, with good agreement between three-dimensional and axisymmetric predictions. They observed that this value of n is larger than the theoretical value, $n = 0.5$ for an infinite single rotating disk, owing to the different nature of the flow.
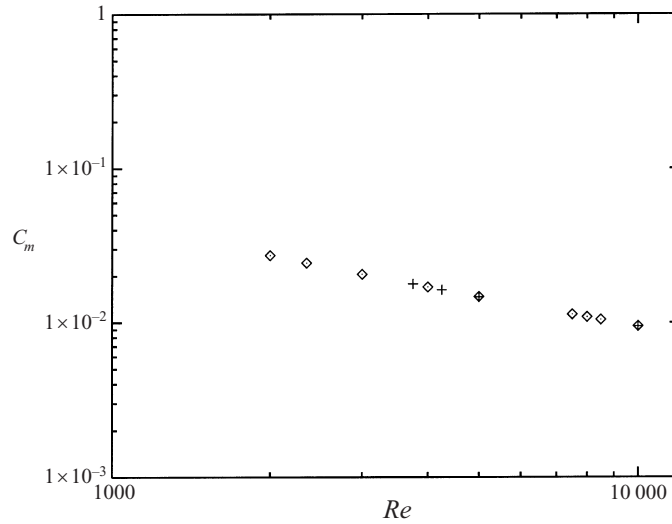
FIGURE 17. Variation of the disk torque coefficient with Reynolds number Re for the $\diamond$, axisymmetric and $+$, three-dimensional solutions: $G = 0.6$.

8. Conclusions

A numerical investigation of the spatio-temporal behaviour of the flow in an enclosed corotating disk pair has been performed with a high-resolution spectral method. Axisymmetric and three-dimensional flow regimes have been analysed, and the different bifurcations occurring in such a geometry have been delineated. The occurrence of unsteady motion has been shown for a range of rotation rates and for values of the aspect ratio less than a critical value $G_c \sim 0.26$, similar to the findings of Tavener *et al.* (1991) for Taylor–Couette problems. This critical limit was found by Herrero *et al.* (1999) to correspond to the separation between two classes of three-dimensional regimes, with symmetry breaking at higher values of G and shift-and-reflect symmetry at lower values. For the transition to three-dimensional regimes, the 'alternating vortex states regime' observed experimentally by Abrahamson *et al.* (1989) is obtained for the largest gap ratio considered ($G = 0.6$). Large vortices in the core region rotate with an angular velocity $\Omega_{II} = 0.697\Omega$, with a wavelength $\lambda = 2\pi/8$, where Ω is the angular velocity of the disks. Multiple solutions develop during the transition, with the presence of quasi-periodic motion resulting from vortex pairings and a predominant monoperiodic state. The flow is characterized by the 'shift-and-reflect' symmetry reported by Herrero *et al.* (1999) with a well-defined polygonal shape of the detached shear layer. Increasing rotation rate leads to a decrease of the number of vortices in the core region and a bifurcation to 'symmetry breaking' structure, in agreement with previous works. Exchanges of fluid between the core region and the inner region occur through spiral arms, owing to the different behaviour of the flow in these regions (see Akhmetov & Tarasov 1987). The variation of torque coefficient as a function of the rotation rate is the same for both the axisymmetric and three-dimensional solutions.

For $G = 0.258$, starting from an unsteady monoperiodic axisymmetric solution, the three-dimensional flow exhibits clearly symmetry breaking with respect to the inter-disk midplane. The vortices in the core region rotate with a drift $\Omega_{II} = 0.6455\Omega$, which comes close to the theoretical value 0.5 found by Humphrey *et al.* (1995) for

$G = 0.279$ at higher rotation rates, and a wavelength $\lambda = 2\pi/3$ owing to its temporal quasi-periodic nature. Such findings are consistent with experimental observations made by Abrahamson *et al.* (1989). Discrepancies with the predictions of Herrero *et al.* (1999) and the data from Humphrey & Gor (1993) may be explained by the difference on the curvature parameters considered.

Computations are now being carried out at higher values of the rotation rate in order to match values in experimental studies carried out at the University of Bath.

REFERENCES

ABRAHAMSON, S. D., EATON, J. K. & KOGA, D. J. 1989 The flow between shrouded corotating disks. *Phys. Fluids* A **1**, 241–251.

AKHMETOV, D. G. & TARASOV, V. F. 1987 Structure and evolution of vortex cores. *J. Appl. Mech. Tech. Phys.* **27**, 690–694.

CANUTO, C., HUSSAINI, M. Y., QUARTERONI, A. & ZANG, T. A. 1987 *Spectral Methods in Fluid Dynamics.* Springer.

CHAOUCHE, A. M., RANDRIAMAMPIANINA, A. & BONTOUX, P. 1990 A collocation method based on an influence matrix technique for axisymmetric flows in an annulus. *Comput. Meth. Appl. Mech. Engng* **80**, 237–244.

DAUBE, O., COUSIN, N., LE QÚERÉ, P. & PÉCHEUX, J. 1994 Sur l'influence des effets de courbure sur la transition à l'instationnarité des écoulements inter-disques. *LIMSI Rep.* 94-10.

FOWLIS, W. W. & HIDE, R. 1965 Thermal convection in a rotating annulus of liquid: effect of viscosity on the transition between axisymmetric and non-axisymmetric flow regimes. *J. Atmos. Sci.* **22**, 541–558.

GAN, X., MIRZAEE, I., OWEN, J. M., REES, D. A. S. & WILSON, M. 1996 Flow in a rotating cavity with a peripheral inlet and outlet of cooling air. In *ASME Intl Gas Turbine Aeroengine Cong., Birmingham* paper 96-GT-309.

GOTTLIEB, D. & ORSZAG, S. A. 1977 *Numerical Analysis of Spectral Methods: Theory and Applications.* CBMS Regional Conf. Series in Appl. Math., SIAM.

HALDENWANG, P., LABROSSE, G., ABBOUDI, S. & DEVILLE, M. 1984 Chebyshev 3-D spectral and 2-D pseudospectral solvers for the Helmholtz equation. *J. Comput. Phys.* **55**, 115–128.

HERRERO, J., GIRALT, F. & HUMPHREY, J. A. C. 1995 Numerical calculation of unsteady 3-D flow between a pair of corotating disks in a fixed enclosure. In *ASME Fluids Engineering Division, IMECE*, vol. 234, pp. 277–285.

HERRERO, J., GIRALT, F. & HUMPHREY, J. A. C. 1999 Influence of the geometry on the structure of the flow between a pair of corotating disks. *Phys. Fluids* **11**, 88–96.

HIGNETT, P., WHITE, A. A., CARTER, R. D., JACKSON, W. D. N. & SMALL, R. M. 1985 A comparison of laboratory measurements and numerical simulations of baroclinic wave flows in a rotating cylindrical annulus. *Q. J. R. Met. Soc.* **111**, 131–154.

HUGUES, S. 1998 Développement d'un algorithme de projection pour méthodes pseudospectrales: application à la simulation d'instabilités tridimensionnelles dans les cavités tournantes. Modélisation d'écoulements turbulents dans les systèmes rotor-stator. Doctorate thesis. Université de la Méditerranée Marseille, France.

HUGUES, S. & RANDRIAMAMPIANINA, A. 1998 An improved projection scheme applied to pseudospec-

tral methods for the incompressible Navier–Stokes equations. *Intl J. Numer. Meth. Fluids* **28**, 501–521.

HUGUES, S., SERRE, E., CRESPO DEL ARCO, E., RANDRIAMAMPIANINA, A. & BONTOUX, P. 1998 Instabilité tridimensionnelle de la couche d'Ekman dans une configuration annulaire avec flux forcé. *C. R. Acad. Sci. Paris* **320**, Sér. IIb, 873–879.

HUMPHREY, J. A. C. & GOR, D. 1993 Experimental observations of an unsteady detached shear layer in enclosed corotating disk flow. *Phys. Fluids* **5**, 2438–2442.

HUMPHREY, J. A. C., SCHULER, C. A. & WEBSTER, D. R. 1995 Unsteady laminar flow between a pair of disks corotating in a fixed cylindrical enclosure. *Phys Fluids* **7**, 1225–1240.

IGLESIAS, I. & HUMPHREY, J. A. C. 1998 Two- and three-dimensional laminar flows between disks co-rotating in a fixed cylindrical enclosure. *Intl J. Numer. Meth. Fluids* **26**, 581–603.

KONIJNENBERG, J. A. VAN DE, NIELSEN, A. H., RASMUSSEN, J. J. & STENUM, B. 1999 Shear-flow instability in a rotating fluid. *J. Fluid Mech.* **387**, 177–204.

LE QUÉRÉ, P. & PÉCHEUX, J. 1990 A three-dimensional pseudo-spectral algorithm for the computation of convection in rotating annulus. *Comput. Meth. Appl. Mech. Engng* **80**, 261–271.

LEWIS, T. W., REES, D. A. S. & WILSON, M. 1998 Unsteady axisymmetric flow in a rotating cavity with a stationary outer surface. In *Proc. Mini Workshop on Appl. Maths, Sylhet, Bangladesh*.

MIRZAEE., I., WILSON, M. & OWEN, J. M. 1997 Heat transfer in a rotating cavity with a peripheral inflow and outflow of cooling air. In *ASME Intl Gas Turbine Aeroengine Cong., Orlando* paper 97-GT-136.

OWEN, J. M. & ROGERS, R. H. 1995 *Flow and Heat Transfer in Rotating Disc Systems: vol. 2. Rotating Cavities*. Research Studies, Taunton, UK.

RANDRIAMAMPIANINA, A., ELENA, L., FONTAINE, J. P. & SCHIESTEL, R. 1997 Numerical prediction of laminar, transitional and turbulent flows in shrouded rotor-stator systems. *Phys. Fluids* **9**, 1696–1713.

RANDRIAMAMPIANINA, A., LEONARDI, E. & BONTOUX, P. 1998 A numerical study of the effects of Coriolis and centrifugal forces on buoyancy driven flows in a vertical rotating annulus. In *Advances in Computational Heat Transfer* (ed. G. De Vald Davis & E. Leonardi), pp. 322–329. Begell House.

SCHULER, C. A., USRY, W. R., WEBER, B., HUMPHREY, J. A. C. & GREIF, R. 1990 On the flow in the unobstructed space between shrouded corotating disks. *Phys. Fluids* A **2**, 1760–1770.

TAVENER, S. J., MULLIN, T. & CLIFFE, K. A. 1991 Novel bifurcation phenomena in a rotating annulus. *J. Fluid Mech.* **229**, 483–497.

TRITTON, D. J. 1988 *Physical Fluid Dynamics*. Clarendon.

VANEL, J. M., PEYRET, R. & BONTOUX, P. 1996 A pseudospectral solution of vorticity-streamfunction equations using the influence matrix technique. In *Numerical Methods in Fluid Dynamics II* (ed. K. W. Morton & M. J. Baines), pp. 463–475. Clarendon.

ZANG, T. A. 1990 Spectral methods for simulations of transition and turbulence. *Comput. Meth. Appl. Mech. Engng* **80**, 209–221.